

MacLaren, I., Wang, L.Q., Schaffer, B., Ramasse, Q.M., Craven, A.J., Selbach, S.M., Spaldin, N.A., Miao, S., Kalantari, K., and Reaney, I.M. (2013) Novel nanorod precipitate formation in neodymium and titanium codoped bismuth ferrite. *Advanced Functional Materials*, 23 (6). pp. 683-689. ISSN 1616-301X

Copyright © 2013 Wiley

A copy can be downloaded for personal non-commercial research or study, without prior permission or charge

The content must not be changed in any way or reproduced in any format or medium without the formal permission of the copyright holder(s)

When referring to this work, full bibliographic details must be given

<http://eprints.gla.ac.uk/78441/>

Deposited on: 17 April 2013

Novel Nanorod Precipitate Formation in Neodymium and Titanium Codoped Bismuth Ferrite

Ian MacLaren,* Li Qiu Wang, Bernhard Schaffer, Quentin M. Ramasse, Alan J. Craven, Sverre M. Selbach, Nicola A. Spaldin, Shu Miao, Kambiz Kalantari, and Ian M. Reaney

The discovery of unusual nanorod precipitates in bismuth ferrite doped with Nd and Ti is reported. The atomic structure and chemistry of the nanorods are determined using a combination of high angle annular dark field imaging, electron energy loss spectroscopy, and density functional calculations. It is found that the structure of the BiFeO₃ matrix is strongly modified adjacent to the precipitates; the readiness of BiFeO₃ to adopt different structural allotropes in turn explains why such a large axial ratio, uncommon in precipitates, is stabilized. In addition, a correlation is found between the alignment of the rods and the orientation of ferroelastic domains in the matrix, which is consistent with the system's attempt to minimize its internal strain. Density functional calculations indicate a finite density of electronic states at the Fermi energy within the rods, suggesting enhanced electrical conductivity along the rod axes, and motivating future investigations of nanorod functionalities.

1. Introduction

There has been tremendous recent research activity on perovskite BiFeO₃ because of its room temperature multiferroism.^[1] Perhaps of equal interest are its ferroelectric properties: it shows one of the largest known electric polarizations

($\approx 90 \mu\text{C cm}^{-2}$), is lead-free, and has a small ($\approx 2 \text{ eV}$) band gap which is likely responsible for recent reports of conducting domain walls^[2] and enhanced photovoltaic behavior.^[3] Chemical modification of BiFeO₃ is proving to be a valuable route to enhancing its properties. For example rare-earth substitution has been shown to increase resistivity by minimizing leakage currents,^[4–7] as well as inducing a crossover from rhombohedral *R3c* to an orthorhombic antipolar PbZrO₃-like *Pbnm* structure enhancing the piezoelectric properties for chemical compositions in the crossover region between.^[8–10] Additional codoping with Ti⁴⁺ has also recently been shown to be highly effective at reducing leakage currents in Nd-doped BiFeO₃,^[11] but over-doping with Ti reduces long range

antipolar ordering and significantly reduces the Curie temperature (T_C) in a nonlinear, and hitherto unknown manner,^[11] and it has recently been shown that this is associated with the creation of novel precipitates with a structure that is not well understood.^[12] Here, we report the formation of self-assembled, coherent precipitates of well-defined Nd nanorods only 2 atomic columns thick. The structure and chemistry of the Nd nanorods is elucidated by scanning transmission electron microscopy combined with first principles calculations. Electronic structure calculations predict the nanorod precipitates to be electrically conducting, demonstrating the possibility of self-assembled, nanometre wide, conducting channels in a resistive, ferroic matrix.

2. Results and Discussion

2.1. Atomic Resolution Imaging and Chemical Mapping of the Nanorods

In Figure 1 we show an atomic resolution high angle annular dark field (HAADF) scanning transmission electron microscopy (STEM) image of [001] oriented BiFeO₃ codoped with $\approx 15\%$ Nd on the A site and $\approx 10\%$ Ti on the B site. The most striking features of the image are the distinctive 8-atom column defects that are approximately evenly spaced in the (001) plane. Similar features are observed throughout the sample. In order to

Dr. I. MacLaren, L.Q. Wang, Dr. B. Schaffer,
Prof. A. J. Craven
SUPA, School of Physics and Astronomy
University of Glasgow
Glasgow G12 8QQ, UK
E-mail: ian.maclaren@glasgow.ac.uk
Dr. B. Schaffer, Dr. Q. M. Ramasse
SuperSTEM Laboratory
Daresbury Science and Innovation Campus
Keckwick Lane, Warrington WA4 4AD, UK
Dr. S. M. Selbach, Prof. N. A. Spaldin
Materials Theory, ETH Zürich
Wolfgang-Pauli-Strasse 27, 8093 Zürich, Switzerland
Dr. S. M. Selbach
Department of Materials Science and Engineering
Norwegian University of Science and Technology
NO-7491 Trondheim, Norway
Dr. S. Miao, Dr. K. Kalantari, Prof. I. M. Reaney
Department of Materials Science and Engineering
University of Sheffield
Sheffield S1 3JD, UK



DOI: 10.1002/adfm.201201835

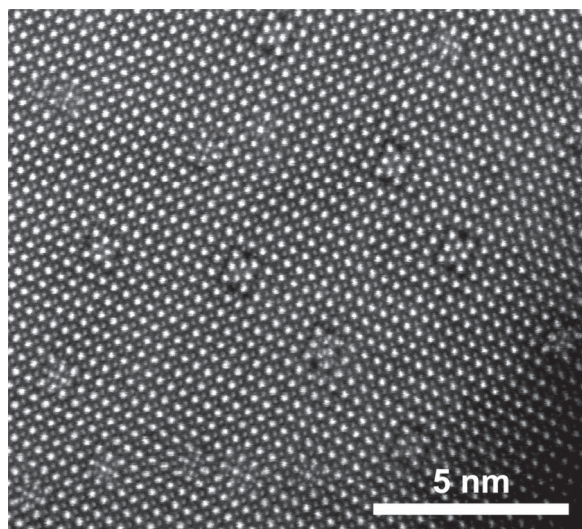


Figure 1. HAADF imaging of nanorod precipitates in an end-on orientation in BiFeO_3 doped with 15% Nd and 10% Ti.

understand these defects in detail, we first applied techniques for quantitative STEM imaging from two orthogonal projections combined with chemical mapping using electron energy loss spectrum imaging (EELS-SI) to provide the data required for the development of a three dimensional model of these defects.

In **Figure 2a** we show an atomic resolution high angle annular dark field (HAADF) scanning transmission electron microscopy of two 8-atom column defects. The bright spots show the positions of the A-site Bi/Nd columns, and the weaker spots the B-site Fe/Ti columns. These defects may also be viewed in the side-on orientation, as shown in **Figure 3a**. (Both **Figure 2a** and **Figure 3a** were created by repeated fast scanning of an area containing the defect, followed by cross correlation and summation to create a high signal-to-noise image with minimal distortion from drift,^[13,14]) In **Figure 3a** the [001] direction of the primitive perovskite cell lies in the sample plane and the viewing direction is [100]. It is clear from this second image that the defects are rod-shaped, with the long axis always oriented along the [001] direction. In addition, the HAADF image shows characteristic additional bright columns of atoms (arrows) lying between the A-site atoms. Further examples of side-view images of these defects are shown in **Figure S5** (Supporting Information), and these defects have a wide range of lengths from just about 3 unit cells (≈ 1.2 nm) up to more than 10 nm; on account of their rod morphology and nanometre scale these are henceforth referred to as nanorods.

To determine the chemistry of the nanorods, we next use atomic resolution chemical mapping using electron energy loss spectrum imaging (EELS-SI). Atomic resolution maps of the elemental distribution of Fe, Ti and Nd derived from an EELS-SI of one nanorod in “top view” (along [001]) are shown in **Figure 2b–e**. The EELS-SI data show clearly that the central part of the nanorod is lacking in B-site cations (Fe/Ti) and that the

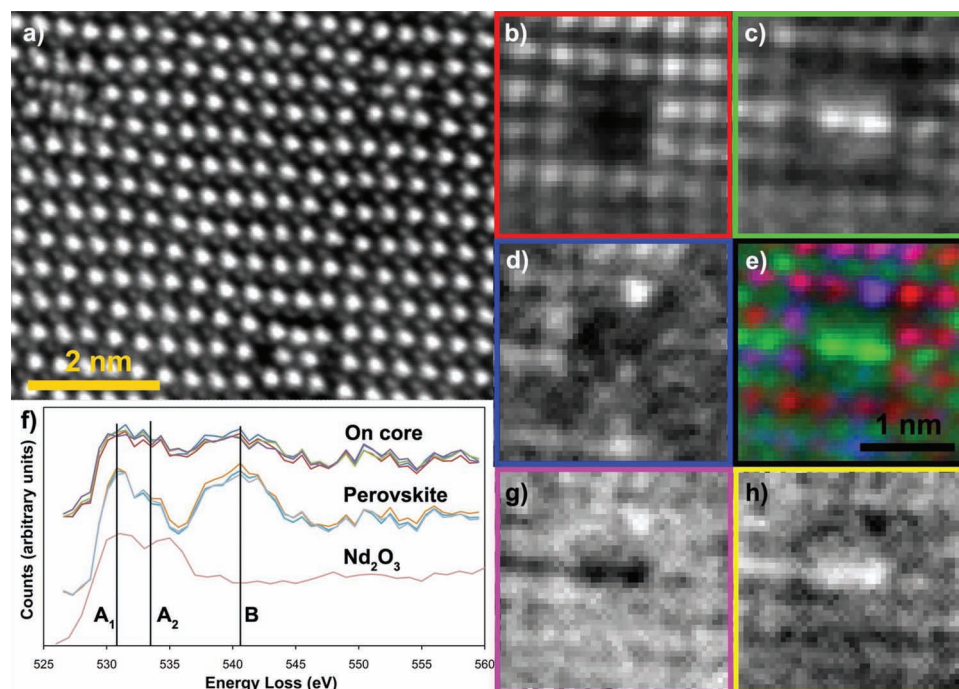


Figure 2. Quantitative imaging and electron energy loss elemental mapping of the nanorods in an end-on orientation; a) HAADF image formed by summing 46 drift-corrected short acquisitions of one area. b–e) elemental maps created from a EELS-SI of one such nanorod: b) Fe map; c) Nd map; d) Ti map; e) RGB map created where red represents Fe, green represents Nd and blue represents Ti; f) O K-edge EELS spectra from the nanorod core, outside the nanorod core and a Nd_2O_3 spectrum for reference; g) MLLS fit coefficient map for the O-K edge shape for bulk perovskite; h) MLLS fit coefficient map for the O-K edge shape for the Nd_2O_3 edge shown in (f).

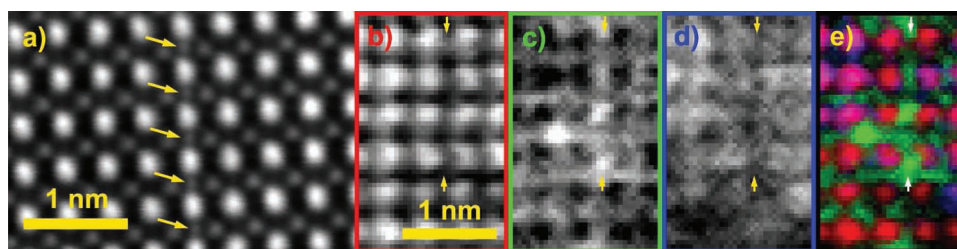


Figure 3. Quantitative imaging and electron energy loss elemental mapping of the nanorods in side-on orientation; a) HAADF image of one such nanorod formed by summing 27 drift-corrected short acquisitions, pairs of Nd atoms along the beam direction are indicated by yellow arrows. b–e) elemental maps created from a EELS-SI of one such nanorod, the nanorod lies between the arrows in all maps: b) Fe map; c) Nd map; d) Ti map; e) RGB map created where red represents Fe, green represents Nd and blue represent Ti.

two central columns are Nd-rich. Nd is also found in other columns around the nanorod, but in smaller and variable quantities consistent with its alloying with Bi in the matrix; spectrum images of regions without nanorods show a random and nonuniform distribution of Nd on the A sites. Most nanorods do not persist through the entire thickness as is discussed further in the Supporting Information with the aid of image simulations. In addition, the electron beam tends to spread significantly after channelling along a heavy column for a few unit cells resulting in significant background signals in both imaging and spectroscopy.^[15] Thus, each atomic column in the spectrum image will also contain unknown contributions from the BiFeO₃ matrix and the chemistry cannot be absolutely quantified from the EELS-SI. The Ti map, Figure 2d, shows that at least one column at the edge of the nanorod is enriched in Ti (see also Figure S4, Supporting Information). Oxygen maps were also created, but revealed little information on precise atomic positions in the nanorods (see the Supporting Information). This lack of resolution of individual atoms probably occurs because of a reduced spatial resolution for the elemental mapping, possibly due to delocalisation of the excitation of the O-K edge.^[16] In the core of the nanorods, the mapping tells us that the nanorods have similar oxygen content to the matrix, but it is difficult to determine the precise location of oxygen in the nanorods.

In order to understand the chemical identity of the atoms in between the A-site positions, EELS-SI was performed on 17 nanorods from the side-on view. An example of a map derived from one of these spectrum images is shown in Figure 3b–e. Figure 3b shows the Fe map, which is similar in the matrix and immediately adjacent to the nanorod core. In contrast, the Nd map (Figure 3c) shows a clear concentration to some sites in the nanorod core. Finally, the Ti map (Figure 3d) indicates a depletion of Ti in the core and a slight enrichment at some sites on the edge of the nanorod. The three-colour RGB overlay reveals that some of the Nd sites at the nanorod core lie in the same plane as the Fe atoms, and not in the main A-site (Bi,Nd) columns. We conclude, therefore, that the “halfway” positions pointed out previously in the HAADF image of Figure 3a are occupied by Nd atoms. We see also that the Nd atoms in the surrounding matrix occupy the expected A-site positions.

Since the EELS-SI oxygen maps reveal relatively little about the oxygen distribution, we next measure the oxygen energy loss near-edge structure (ELNES) to investigate the oxygen local bonding in the nanorods. In Figure 2f we compare the struc-

ture of the O K-edge in the nanorod core using a spectrum summed from a selected 7×7 square of pixels of the spectrum image centred around a Nd column and the same selection size around an expected column position for the oxygen in the perovskite matrix at the top of the image, in each case recording background subtracted O K-edge spectra in three different locations. For comparison a reference spectrum from Nd₂O₃ is also shown.^[17] We find significant differences between the nanorod and matrix spectra. As expected, the spectra from the matrix correspond well to the spectra from bulk doped BiFeO₃ (see for instance Saeterli et al.^[18]). The Nd-rich core, in contrast, gives an A₂ peak of similar height to the A₁ peak and the whole O post-edge region after the A₁ and A₂ peaks is flatter than for the matrix. This is consistent with previously recorded spectra for Nd₂O₃ where the A₁ and A₂ peaks are of similar height and the B peak is weaker, and this suggests that the core of the nanorod is chemically similar to neodymium oxide. To show this local variation visually we next map the local chemistry from the EELS-SI using multiple linear least squares (MLLS) fitting. This was done by fitting the observed O K edge shape at each point in the spectrum image as a linear combination of our measured O-K edge profile from the BiFeO₃ matrix and a Nd₂O₃ standard electron energy loss spectrum.^[17] Figure 2g shows the fit coefficient for the BiFeO₃ matrix and Figure 2h shows the fit coefficient for the Nd₂O₃ standard. The similarity between the O bonding map of Figure 2h (for Nd₂O₃) and the Nd elemental map of Figure 2c confirms the chemical similarity of the nanorod core to Nd₂O₃.

2.2. The 3-Dimensional Structure of the Nanorods

In view of the fact that the exact positions of the oxygen atoms could not be determined experimentally, next we use density functional theory within the local density approximation plus Hubbard U method to calculate the lowest energy arrangement of the atoms. We begin by measuring the positions of the bright A-site (i.e., Bi/Nd) columns from HAADF images of six different nanorods and averaging. The average uncertainty for A-site positions in the nanorods was then ≈ 14 pm. The full details of average atomic positions and standard deviations are given in the Supporting Information (Figure S2 and Table S1). Our resulting model has 2 columns of Nd ions surrounded by a matrix of bulk-like BiFeO₃, which is very distorted close to the

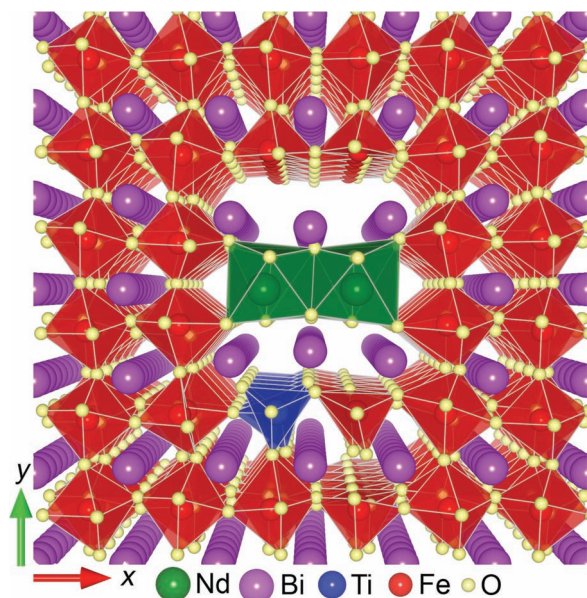


Figure 4. Atomic structure model after DFT structural relaxations in end-on orientation.

Nd core. In accordance with the chemical mapping, we then placed the Ti ions in the B-site columns of the matrix BiFeO_3 adjacent to the Nd columns. To choose the number of oxygen ions we took the formal charges of Nd^{3+} , Bi^{3+} , Fe^{3+} , and Ti^{4+} , and added a stoichiometric number of oxygen ions to maintain charge balance. We constructed a large number of possible starting supercell models with different local arrangements of oxygen ions, focusing on the coordination of Nd and Ti, and different positions of the Ti ions (in the same or neighboring columns). The atomic positions were then relaxed fully using density functional theory (DFT). Note that, since our calculated supercell matrix does not contain Nd, our structural optimizations obtained the $a^-a^-a^-$ octahedral tilt structure of undoped BiFeO_3 ; when we imposed the $a^-a^-c^0$ pattern of the PbZrO_3 -type structure found in samples with this level of Nd doping, (which we could not subsequently allow to relax) we obtained the same qualitative behavior that we present here. (Doping of the matrix with Nd was not included in our calculations due to the extra complexity this would introduce in the DFT calculations).

Our lowest energy calculated nanorod/matrix is shown in **Figure 4**. To confirm its validity, we simulated its HAADF image using the frozen phonon treatment of thermal diffuse scattering within the QSTEM multislice simulation package.^[19] Excellent qualitative agreement between the simulated and measured images was obtained (Figure S10, Supporting Information). Perhaps the most striking structural feature of our calculated structures is the presence of (Fe/Ti)- O_5 square-based pyramids containing five-coordinated Fe/Ti ions immediately adjacent to the Nd-rich core; in contrast bulk BiFeO_3 contains FeO_6 octahedra. We find that oxygen atoms have transferred from the FeO_6 octahedra to the Nd-rich core, so that the Nd ions become seven-coordinated. This is accompanied by significant off-centering of the B-site ions, especially the Fe ions above the Nd-rich core, which reproduces contrast in image simulations very much like the experimental observations (Figure S10, Supporting

Information). We find that this configuration of five-coordinated Fe/Ti and seven-coordinated Nd has lower energy than corner-sharing NdO_6 and FeO_6 octahedra. One origin of this configuration is likely chemical: the larger and more electropositive Nd^{3+} ions have a greater affinity for oxygen ions than Fe^{3+} ions do, and while Nd^{3+} is commonly found with a coordination number of 6 or higher in oxides, the coordination number of Fe^{3+} is usually 6 or lower (see the Supporting Information, Figures S7–9 for further discussion of these points). We note also that the FeO_5 square pyramids we find here are reminiscent of the so-called T-phase that is commonly found in strained thin films of BiFeO_3 .^[20,21] Here, the “internal strain” caused by the cores of the nanorods, which contain only two A-site cations where there would be three in bulk BiFeO_3 , appears to induce an analogous local phase change on the surrounding cells of perovskite BiFeO_3 . Conversely, the ability of BiFeO_3 to adapt to the anisotropic local strain by morphing smoothly between structural allotropes likely facilitates the spontaneous formation of the nanorods, where their formation in a “harder” matrix material would introduce prohibitively large local strains. Indeed, super-saturated solid solutions usually form spherical rather than rod-shaped precipitates because the former minimize the unfavorable interfacial energy. The fact that rod-shaped precipitates have formed here suggests a significantly lower interfacial energy between the core and the matrix. We note that local regions of T-phase have also been reported at the BiFeO_3 - Bi_2O_3 interface in thin films^[22] and are predicted theoretically in Fe-doped Bi-based Aurivillius phase compounds.^[23] The local tensile strain may also favor segregation of the smaller Ti^{4+} ions towards the nanorod/matrix interface, where configurational entropy would favor a random distribution of Ti in the matrix, although here the compensation of the higher valence Ti^{4+} B-site cations by the A-site vacancies likely also plays a role. As noted in the Supporting Information, the DFT calculations show that segregation of Ti to one column around the nanorod is energetically favorable in agreement with the experimental results such as Figure 1d. Indeed, as discussed in more detail elsewhere,^[12] the very formation of the nanorods is likely caused by the creation of A-site vacancies, specifically exsolving a proportion of the Nd^{3+} , as an ionic compensation mechanism associated with the doping of an excess of Ti^{4+} into the ceramic.

2.3. Properties of the Nanorods and their Effects on the Perovskite Matrix

2.3.1. Strain Interactions with the Matrix, Spontaneous Alignment and Domain Pinning

In addition to the interplay between strain and local B-site coordination, it is likely that the observed parallel alignment of the nanorods is caused by minimization of strain energy in the system. Our observation (see the Supporting Information for micrographs and diffraction patterns) that the precipitates are always parallel to specifically the [001] axis of the P_{bam} BiFeO_3 matrix is of particular interest since the nanorods form at high temperature during sintering, whereas the ferroelastic domain structure forms in a phase transition from a paraelectric (PE) P_{bnm} structure to antiferroelectric (AFE) P_{bam} structure

transition at ≈ 250 °C.^[11] At the PE-AFE transition the cell doubles along the *b* axis and there is a volume change of $\approx 2\%$ dominated by an anisotropic expansion of the pseudocubic *b* axis.^[10] It is likely, therefore that the nanorods formed parallel to the [001] axis in the high temperature *Pbnm* phase (also sometimes referred to in an alternate cell setting as *Pnma*^[24]) and that this specific alignment is energetically favored by strain considerations. Whilst it is unclear whether the growth of ferroelastic domains in the AFE structure is purely determined by the domain structure in the PE structure, or whether the additional strain fields of the nanorods also plays a role, it is likely that the presence of these aligned strain fields from the nanorods will strongly influence domain alignment and make AFE-FE switching more difficult. Moreover, if the parallel nanorods could be generated in an FE composition, the nanorods will act as pinning centres for domain wall motion under applied field, hardening the FE behavior. The PE-FE transition also shows a large volume change and it is anticipated that similar domain-precipitate alignment is feasible. Their presence and configuration therefore hints at subtle ways in which domain structures in RE-doped BiFeO₃ may be engineered, a subject of potential importance for thin film applications.

2.3.2. Electronic Properties of the Nanorods

Finally, we use density functional theory to calculate the electronic properties of our nanorods. Our calculated local densities of states (DOS) are shown in Figure 5. We find that the electronic structure of the nanorods and the adjacent interface layer deviates strongly from that of the BiFeO₃ matrix. In particular, the nanorods have a finite DOS at the Fermi energy indicating that we should expect them to be more electrically conducting than the BiFeO₃ matrix. Bi *p* states dominate the electronic structure at E_F , with contributions from Bi *s*, O *p* and Nd *d* states (see the Supporting information). In addition, the band gap is reduced to 0.8 eV in the interfacial BiFeO₃ region immediately next to the Nd oxide core (Figure 5b). The origin of the reduction is the lowering in energy of the Fe *d* states at the bottom of the conduction band due to the reduction in crystal field splitting. The electronic structure of the matrix region is very similar to that of bulk BiFeO₃ from our own calculations (Figure 5c) and previous studies^[25] and shows the calculated literature band gap of ≈ 2.0 eV. While in our current study the matrix is antipolar *Pbam*, we expect that similar precipitates will form in compositions with $<15\%$ Nd which are reported to be ferroelectric and rhombohedral.^[11] Conducting self-assembled parallel nanorods in a ferroelectric matrix could open intriguing new device directions, and verification of our predicted electrical properties will be the focus of future work.

2.3.3. Possible Magnetic Effects of the Nanorods

The presence of the nanorods may also have some influence on magnetic properties. Kalantari et al.^[11] have reported that Ti-doping in the B-site of the ABO₃ perovskite lattice decreases T_N monotonically. However, there is a small lattice distortion associated with T_N whose latent heat is visible by differential scanning calorimetry.^[11] Local strain centres surrounding the nanorods may therefore influence the precise configuration of

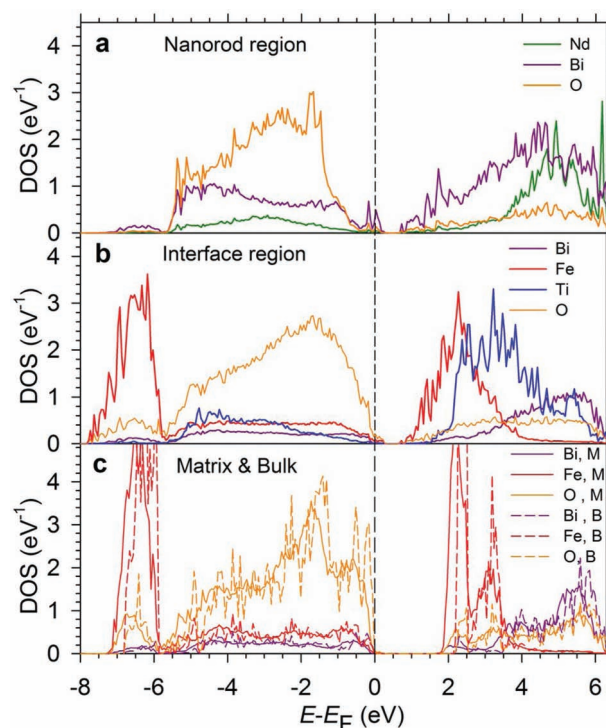


Figure 5. Calculated local electronic structure: a) Atomic densities of states (DOS) of the Nd-O nanorod and the 6 Bi atoms per layer closest to the nanorod; b) Atomic DOS for the BiFe(Ti)O₃ unit cell layer at the interface towards the Nd nanorod; c) Atomic DOS for the matrix of the supercell (M) compared with the DOS of bulk BiFeO₃ (B). The DOS are scaled to one formula unit.

the local magnetic dipolar order. The magnetic structure of the nanorods and its influence the surrounding perovskite and the bulk magnetic properties requires further study.

3. Conclusions

We have demonstrated the spontaneous formation and self-assembly of Nd-rich nanorods in BiFeO₃ codoped with Nd and Ti. We characterised the structure of the nanorods and the surrounding interfacial region using a combination of atomic resolution imaging and spectroscopy in the scanning transmission electron microscope and density functional calculations. Our calculations suggest an interplay between strain and structure in the nanorods and surrounding matrix, with (i) the nanorods stabilized by and/or inducing the formation of local “T-phase” BiFeO₃ in the interfacial region, and (ii) the spontaneous alignment of the nanorods correlating with the domain structure in the BiFeO₃ matrix. Electronic structure calculations predict that the nanorods have higher electrical conductivity than the surrounding, insulating matrix, paving the way to additional novel functionalities in multiferroic BiFeO₃.

4. Experimental Section

Materials Synthesis and TEM Sample Preparation: Ceramic specimens with a nominal composition of Bi_{0.85}Nd_{0.15}Fe_{0.9}Ti_{0.1}O₃ were fabricated by

a mixed oxide route from Bi_2O_3 , Nd_2O_3 , Fe_2O_3 and TiO_2 precursors by calcination at 1020 °C for 3 h and sintering at 1050 °C for 3 h. Fuller details are given elsewhere.^[11]

Specimens were prepared for transmission electron microscopy using a conventional procedure of sawing, mechanical thinning, dimpling, and ion beam thinning, followed by coating with a thin (few nm), even layer of carbon to prevent charging under the electron beam during microscopy. Suitable areas for HR-STEM were identified using conventional transmission electron microscopy using diffraction and imaging with a Tecnai T20 (FEI, Eindhoven, Netherlands) operated at 200 kV.

Scanning Transmission Electron Microscopy: High resolution scanning transmission electron microscopy was performed at the SuperSTEM facility using the Nion UltraSTEM microscope operated at an accelerating voltage of 100 kV. The beam convergence semiangle was 30 mrad and the HAADF detector had an inner radius of 70 mrad and an effective outer radius of 180 mrad. HAADF images for quantitative structure measurements were recorded rapidly at about 10 μs per pixel with multiple repeated scanning in a movie mode, followed by alignment and summation using the SDS software.^[26] Atomic positions were quantitatively measured using the iMtools software,^[27] and were then corrected for the effects of scanning distortions in a similar manner to a previous publication.^[14] Further details of the precise procedure are included in the Supporting Information.

EELS-SI datasets were recorded using dwell times of between 0.05 and 0.2 s per pixel and a dispersion of 0.7 eV/channel using a Gatan spectrometer with an acceptance semiangle of 31 mrad. To reduce the amount of noise in maps, the spectrum images were processed using Principal Component Analysis using the software tool of Watanabe.^[28] For the maps shown in this paper, it was found that about 10–20 components were usually sufficient to separate the elemental signals from the noise effectively. Maps were created using the procedure set out in more detail in the Supporting Information and are normalised for the total signal entering the spectrometer and are smoothed using a weak low pass filter to minimise noise in the final maps, although the raw maps are also displayed in the Supporting Information.

Density Functional Theory: Density functional theory calculations were performed with the VASP code^[29,30] using the Dudarev implementation of GGA + U,^[31,32] with a U_{eff} of 4 eV on Fe. We used projector augmented wave^[33] (PAW) method with the Bi_d, Ti_sv, Fe_pv and O standard PBE potentials supplied with VASP. The f -electrons of Nd were kept frozen in the core by using the special Nd_3 PBE potential. A $\text{Nd}_4\text{Bi}_{66}\text{Ti}_{12}\text{Fe}_{62}\text{O}_{202}$ supercell was constructed to model the Nd nanorod precipitates, together with the surrounding interface and matrix BiFeO_3 , where antiferromagnetic G-type order was imposed. We used a $1 \times 1 \times 3$ Γ -centred k-point grid to sample the Brillouin zone and the plane-wave cutoff energy was set to 500 eV. The Bi and Nd ions were kept at positions obtained from HAADF images during structural relaxations with fixed experimental lattice vectors of $23.79 \text{ \AA} \times 23.79 \text{ \AA} \times 7.81 \text{ \AA}$,^[10] while the Fe, Ti and O ions were relaxed until the forces were $< 0.05 \text{ eV \AA}^{-1}$.

Supporting Information

Supporting Information is available from the Wiley Online Library or from the author.

Acknowledgements

This project would not have been possible without the generous support of the EPSRC in the form of support for the SuperSTEM facility (EP/D040205/1, EP/D040396/1, EP/D040566/1) including the PDRA position held by B.S., funding of a grant to I.M. to allow access to SuperSTEM (EP/I000879/1), provision of a DTA studentship to L.Q.W., and funding of the multiferroic ceramics at Sheffield (EP/G069069/1 and

EP/G005001/1) including a PDRA position for S.M. N.S. and S.M.S. were supported by ETH Zürich. S.M.S. acknowledges financial support from the Strategic Area MATERIALS at NTNU. We are indebted to Dr. Lothar Houben at the FZ-jülich for the provision of the iMtools software used for the quantitative image analysis, together with helpful discussions concerning its use. We are also grateful to Prof. Christoph Koch at the University of Ulm for assistance in setting up the multislice HAADF image simulations using QSTEM. We would also like to thank Dr. Alison Hatt at the Laurence Berkeley National Laboratory for helpful discussions and suggestions concerning the DFT calculations.

Received: July 4, 2012

Published online: September 7, 2012

- [1] G. Catalan, J. F. Scott, *Adv. Mater.* **2009**, *21*, 2463.
- [2] J. Seidel, L. W. Martin, Q. He, Q. Zhan, Y. H. Chu, A. Rother, M. E. Hawkrige, P. Maksymovych, P. Yu, M. Gajek, N. Balke, S. V. Kalinin, S. Gemming, F. Wang, G. Catalan, J. F. Scott, N. A. Spaldin, J. Orenstein, R. Ramesh, *Nat. Mater.* **2009**, *8*, 229.
- [3] T. Choi, S. Lee, Y. J. Choi, V. Kiryukhin, S. W. Cheong, *Science* **2009**, *324*, 63.
- [4] X. D. Qi, J. Dho, R. Tomov, M. G. Blamire, J. L. MacManus-Driscoll, *Appl. Phys. Lett.* **2005**, *86*, 3.
- [5] G. W. Pabst, L. W. Martin, Y. H. Chu, R. Ramesh, *Appl. Phys. Lett.* **2007**, *90*, 3.
- [6] Z. X. Cheng, X. L. Wang, H. Kimura, K. Ozawa, S. X. Dou, *Appl. Phys. Lett.* **2008**, *92*, 092902.
- [7] S. Karimi, I. M. Reaney, I. Levin, I. Sterianou, *Appl. Phys. Lett.* **2009**, *94*, 12903.
- [8] S. Fujino, M. Murakami, V. Anbusathaiah, S. H. Lim, V. Nagarajan, C. J. Fennie, M. Wuttig, L. Salamanca-Riba, I. Takeuchi, *Appl. Phys. Lett.* **2008**, *92*, 3.
- [9] D. Kan, L. Palova, V. Anbusathaiah, C. J. Cheng, S. Fujino, V. Nagarajan, K. M. Rabe, I. Takeuchi, *Adv. Funct. Mater.* **2010**, *20*, 1108.
- [10] I. Levin, S. Karimi, V. Provenzano, C. L. Dennis, H. Wu, T. P. Comyn, T. J. Stevenson, R. I. Smith, I. M. Reaney, *Phys. Rev. B* **2010**, *81*, 020103.
- [11] K. Kalantari, I. Sterianou, S. Karimi, M. C. Ferrarelli, S. Miao, D. C. Sinclair, I. M. Reaney, *Adv. Funct. Mater.* **2011**, *21*, 3737.
- [12] I. M. Reaney, I. MacLaren, L. Q. Wang, B. Schaffer, A. Craven, K. Kalantari, I. Sterianou, S. Karimi, D. C. Sinclair, *Appl. Phys. Lett.* **2012**, *100*, 182902.
- [13] K. Kimoto, T. Asaka, X. Z. Yu, T. Nagai, Y. Matsui, K. Ishizuka, *Ultramicroscopy* **2010**, *110*, 778.
- [14] I. MacLaren, R. Villaurrutia, B. Schaffer, L. Houben, A. Pelaiz-Barranco, *Adv. Funct. Mater.* **2012**, *22*, 261.
- [15] P. D. Robb, M. Finnie, P. Longo, A. J. Craven, *Ultramicroscopy* **2012**, *114*, 11.
- [16] L. J. Allen, A. J. D'Alfonso, S. D. Findlay, J. M. LeBeau, N. R. Lugg, S. Stemmer, *J. Phys.: Conf. Ser.* **2010**, *241*, 012061.
- [17] C. C. Ahn, O. L. Krivanek, *EELS Atlas - A Reference Guide of Electron Energy Loss Spectra Covering All Stable Elements*, **1983**, ASU HREM Facility & Gatan Inc.: Warrendale, PAUSA.
- [18] R. Saeterli, S. M. Selbach, P. Ravindran, T. Grande, R. Holmestad, *Phys. Rev. B* **2010**, *82*, 064102.
- [19] C. Koch, **2002**, PhD Thesis: Arizona State University.
- [20] R. J. Zeches, M. D. Rossell, J. X. Zhang, A. J. Hatt, Q. He, C. H. Yang, A. Kumar, C. H. Wang, A. Melville, C. Adamo, G. Sheng, Y. H. Chu, J. F. Ihlefeld, R. Erni, C. Ederer, V. Gopalan, L. Q. Chen, D. G. Schlom, N. A. Spaldin, L. W. Martin, R. Ramesh, *Science* **2009**, *326*, 977.
- [21] A. J. Hatt, N. A. Spaldin, C. Ederer, *Phys. Rev. B* **2010**, *81*, 054109.
- [22] H. J. Liu, P. Yang, K. Yao, K. P. Ong, P. Wu, J. Wang, *Adv. Funct. Mater.* **2012**, *22*, 937.

- [23] Y. Birenbaum, C. Ederer, **2012**, *Personal Communication*.
- [24] S. Karimi, I. M. Reaney, Y. Han, J. Pokorny, I. Sterianou, *J. Mater. Sci.* **2009**, *44*, 5102.
- [25] J. B. Neaton, C. Ederer, U. V. Waghmare, N. A. Spaldin, K. M. Rabe, *Phys. Rev. B* **2005**, *71*, 014113.
- [26] B. Schaffer, W. Grogger, G. Kothleitner, *Ultramicroscopy* **2004**, *102*, 27.
- [27] L. Houben, **2009**, <http://www.er-c.org/centre/software/imtools.htm> (last accessed August 2012).
- [28] M. Bosman, M. Watanabe, D. T. L. Alexander, V. J. Keast, *Ultramicroscopy* **2006**, *106*, 1024.
- [29] G. Kresse, J. Furthmüller, *Phys. Rev. B* **1996**, *54*, 11169.
- [30] G. Kresse, D. Joubert, *Phys. Rev. B* **1999**, *59*, 1758.
- [31] J. P. Perdew, K. Burke, M. Ernzerhof, *Phys. Rev. Lett.* **1996**, *77*, 3865.
- [32] S. L. Dudarev, G. A. Botton, S. Y. Savrasov, C. J. Humphreys, A. P. Sutton, *Phys. Rev. B* **1998**, *57*, 1505.
- [33] P. E. Blochl, *Phys. Rev. B* **1994**, *50*, 17953.